Research Square

Preprints are preliminary reports that have not undergone peer review.
They should not be considered conclusive, used to inform clinical practice,
or referenced by the media as validated information.

Programmable decoding of stimulus duration directs functional differentiation in synthetic cells

Liang Yue

yueliang2021@hnu.edu.cn

Hunan University https://orcid.org/0000-0002-7915-834X

Si Chen

Hunan University

Huiping Ouyang

Hunan University

Shan Wang

Hunan university https://orcid.org/0000-0001-9014-9981

Article

Keywords:

Posted Date: November 17th, 2026

DOI: https://doi.org/10.21203/rs.3.rs-10775109/v1

License: This work is licensed under a Creative Commons Attribution 4.0 International License.
Read Full License

Additional Declarations: There is **NO** Competing Interest.

Programmable decoding of stimulus duration directs functional differentiation in synthetic cells

Si Chen,[a] Huiping Ouyang,[a] Shan Wang,[a,*] Liang Yue[a,b,*]

[a]Molecular Science and Biomedicine Laboratory (MBL), State Key Laboratory of Chemo and Biosensing, College of Chemistry and Chemical Engineering, Aptamer Engineering Center of Hunan Province, Hunan University, Changsha, Hunan 410082, P. R. China

[b]State Key Laboratory of Synthetic Biology, Tianjin University, 92 Weijin Road, Nankai District, Tianjin 300072, P. R. China

*Email: wangshan21@hnu.edu.cn; yueliang2021@hnu.edu.cn

Abstract

Living systems decode stimulus durations into distinct molecular states and functions. Reconstituting such temporal information processing in chemical systems is challenging because duration is a history-dependent property that cannot be defined by the instantaneous input state. Here we develop a programmable duration-decoding framework within synthetic cells that transforms stimulus durations into molecular decisions and functional behaviours through duration transduction, molecular decision-making, and functional coupling. Duration is transduced via two strategies: integration, where molecular accumulation records input persistence, and filtering, where competing kinetics reject transient signals below tunable persistence thresholds. Downstream nonlinear networks classify figthese trajectories into discrete molecular states, with network topologies and kinetics reconfigured to program duration-to-state mappings. Coupling these states to effectors enables stimulus duration to specify synthetic-cell behaviours spanning transcription, translation, and membrane permeabilisation. These results establish how reaction-network dynamics convert temporal history into molecular states and functions, providing a chemical basis for programmable temporal information processing.

Introduction

A central challenge in constructing cell-like chemical systems is to understand how environmental information is sensed, processed, and translated into functional outcomes.[1–4] Living cells decode information not only from the identity and magnitude of a stimulus but also from its temporal features,[5–8] such as duration.[9] Although synthetic cells have advanced substantially in response to diverse physicochemical stimuli,[10–13] including chemical,[14–16] optical,[17,18] and thermal inputs,[19] these systems predominantly process instantaneous input states rather than explicitly decoding the temporal features of stimuli. The distinction between an input's instantaneous state and temporal structure is fundamental, since temporal features cannot be determined from a single input state but depend on how the input evolves over time. Consequently, how the temporal features of stimuli can be chemically transduced, processed and coupled to functions in synthetic cells remains unresolved.

Among temporal features, duration is a key determinant of cellular output,[20–22] often governing which downstream responses are activated and which functional states are selected. Such duration decoding is evident across biological scales from photoperiodic physiology[23] to mammalian signalling.[24,25] For instance, cellular signalling networks can distinguish transient from sustained activation through their intrinsic reaction dynamics, converting signal durations into distinct downstream regulatory states and ultimately phenotypic outcomes. This illustrates a general information-processing principle: cellular functions are determined not only by what a signal is and how strong it is, but critically by how long it persists. Reconstituting this principle in bottom-up synthetic cells poses a chemical design challenge beyond conventional stimulus-response systems, because molecular systems must transform stimulus duration into internal molecular representations, classify these representations into discrete decision states, and couple the resulting states to distinct functions.

Natural signalling networks address these requirements through a hierarchy of kinetic and regulatory operations. Stimulus-duration decoding often begins with temporal input transduction, in which stimulus duration is converted into chemically readable molecular variables through kinetic operations, such as temporal integration[26,27] and temporal filtering.[28,29] Integration allows molecular intermediates to accumulate during continued stimulation, thereby mapping stimulus duration onto intermediate abundance or activity. Filtering, by contrast, uses kinetic gates or competing reaction pathways to reject short-lived inputs that fall below a prescribed persistence threshold, ensuring that only signals elicited by sufficiently sustained stimulation are relayed. The resulting duration-dependent molecular representations, including abundance, activity, and assembly state,

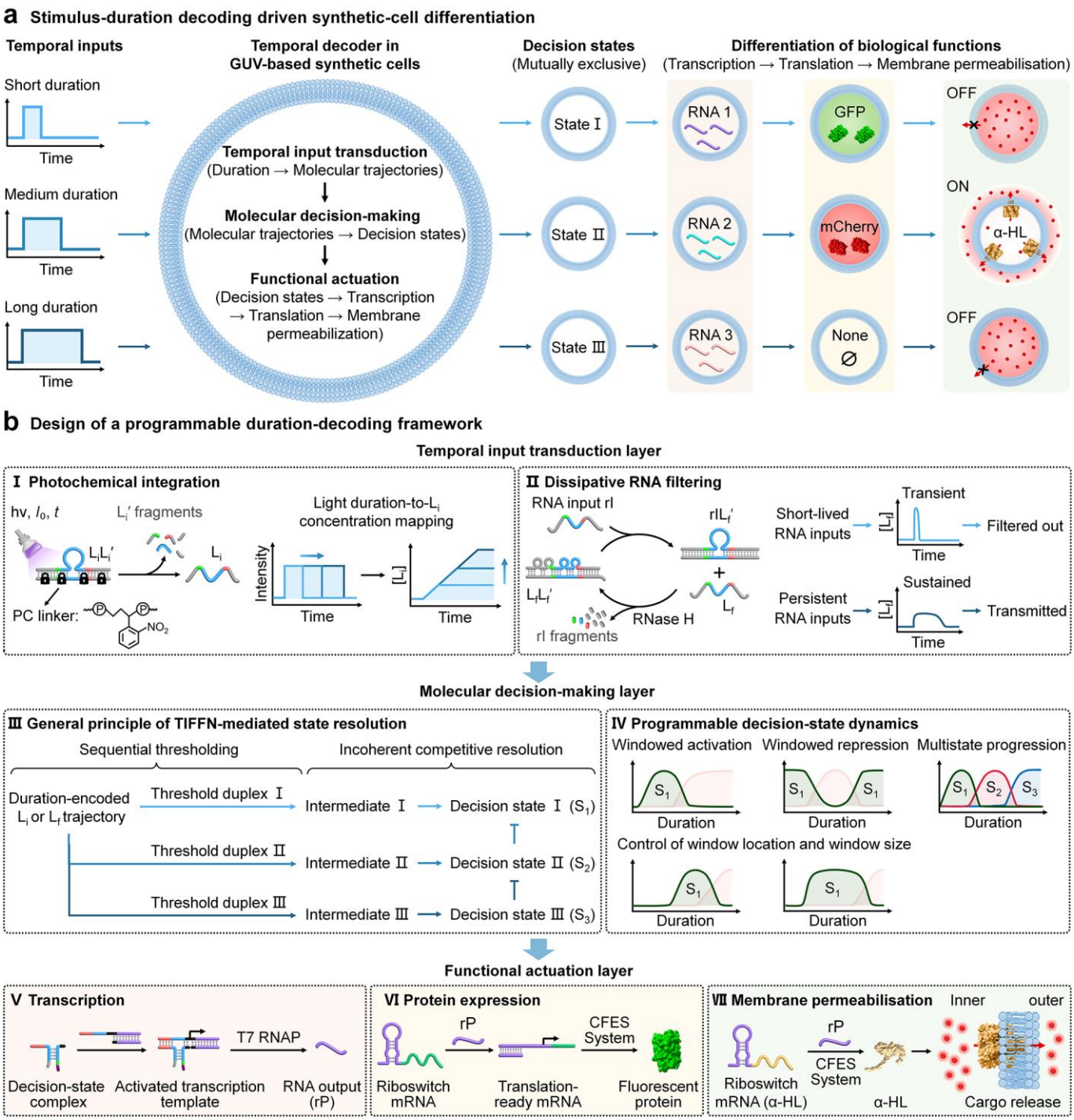


Fig. 1 | A programmable framework for decoding stimulus duration into synthetic-cell decision states and functional outputs. a, Conceptual overview of programmable stimulus-duration decoding in synthetic cells. Temporal inputs with different durations are processed by a DNA-based temporal decoder within giant unilamellar vesicles (GUVs), where stimulus duration is first transduced into programmable molecular trajectories and subsequently decoded into mutually exclusive molecular decision states. These decision states drive transcription, protein expression, and membrane permeabilisation, enabling distinct duration-dependent synthetic-cell functions. **b**, Schematic showing the design of a programmable duration-decoding framework consisting of three modular layers. In the temporal input transduction layer, diverse temporal inputs are transduced into programmable molecular trajectories through two complementary mechanisms. Specifically, photochemical integration progressively accumulates free DNA signal as cumulative molecular trajectories in proportion to light duration (I), whereas dissipative RNA filtering selectively transmits sufficiently persistent RNA inputs to generate persistence-encoded molecular trajectories while suppressing transient inputs (II). In the molecular decision-making layer, programmable threshold-gated incoherent feedforward networks (TIFFNs) resolve duration-encoded molecular trajectories into mutually exclusive decision states through sequential thresholding and incoherent competitive resolution (III). Reconfiguring TIFFN topology and kinetics reshapes the trajectory-to-state transfer function, enabling programmable decision-state dynamics, including windowed activation, windowed repression, multistate progression, and programmable control over response-window location and size (IV). In the functional actuation layer, decoded decision states are coupled to transcription (V),

riboswitch-controlled protein expression (VI) and α-hemolysin (α-HL)-mediated membrane permeabilisation (VII), propagating stimulus-duration decoding into programmable synthetic-cell functions.

provide a chemical representation of temporal history that can be interpreted by downstream regulatory networks. Embedded feedback, feedforward, and thresholding motifs then classify these duration-dependent molecular representations into discrete decision states. Coupling these states to downstream effectors ultimately converts duration into distinct transcriptional programs, phenotypic states or other functional outcomes.[30,31] Guided by this biological logic, reconstituting duration decoding in synthetic cells requires a molecular architecture that integrates temporal input transduction, molecular decision-making, and functional actuation.

In DNA reaction networks,[32–35] sequence-defined base pairing,[36] strand-displacement reactions,[37,38] and enzyme-mediated transformations[39–41] provide programmable control over molecular connectivity and reaction kinetics. This programmability enables external signals to be transformed, routed and integrated through modular reaction pathways, providing a versatile basis for molecular information processing.[42,43] Crucially, the information-processing behaviour of these networks is programmable, with reaction kinetics, activation thresholds, and signal-routing pathways tunable through sequence design,[44] toehold strength,[45] enzyme-recognition sites,[46] and network topology.[47,48] Also, DNA reaction networks can couple processed molecular signals to downstream functions, including condensate assembly,[49] transcription,[50] and protein expression.[19] Together, these capabilities make DNA reaction networks an attractive chemical foundation for constructing programmable information-processing architectures in synthetic cells.

Here, we establish a programmable duration-decoding framework in synthetic cells that translates stimulus duration into discrete molecular decision states, thereby enabling duration-guided functional differentiation (Fig. 1a). This framework consists of three coupled layers: temporal input transduction, molecular decision-making, and functional actuation, creating a modular architecture in which duration sensing, molecular state selection and functional output can be programmed independently while remaining chemically integrated. Within this architecture, temporal integration and temporal filtering serve as complementary input-transduction mechanisms, converting the duration of optical and chemical stimuli, respectively, into duration-dependent molecular trajectories. Downstream nonlinear networks then resolve these trajectories into discrete decision states, while changes in network topology and kinetics enable duration-to-state mappings to be reprogrammed. Coupling these states to downstream gene-expression machinery creates programmable temporal windows for transcription and protein expression. Furthermore, we extend this temporal-control logic to membrane-level actuation by using the selected decision states to control α-hemolysin (α-HL) synthesis. This enables duration-windowed cargo release through α-HL-mediated membrane permeabilisation, extending temporal decision-making from gene expression to membrane-level function. Overall, this work establishes a reaction-network principle for temporal information processing, enabling synthetic cells to translate stimulus durations into discrete molecular decisions and differentiated functional states.

Results and discussion

Design principles of the programmable duration-decoding framework

We established a programmable duration-decoding framework in synthetic cells that converts stimulus duration into molecular decision states to direct functional differentiation (Fig. 1b). This framework is organised into three chemically coupled but functionally distinct layers: temporal input transduction, molecular decision-making and functional actuation. The input-transduction layer converts stimulus durations into DNA-signal trajectories through either temporal integration or temporal filtering. The molecular decision-making layer resolves these trajectories into discrete decision states via threshold-gated incoherent feedforward networks (TIFFNs).[48] The actuation layer uses the resulting states to drive transcriptional, translational, and membrane-level functions. To examine whether this framework could operate with distinct inputs, we implemented temporal integration with light and temporal filtering using an RNA trigger.

To implement temporal integration, we designed a photocleavable DNA duplex, L_iL_i', as a light-transduction module (Fig. 1b, panel I). In this construct, strand L_i' incorporates four photocleavable (PC) linkers,[51,52] while L_i functions as a readable DNA signal for downstream processing. Under fixed irradiance and within the calibrated operating regime, continued illumination progressively cleaves L_i', thus destabilising duplex L_iL_i' and releasing L_i in a duration-dependent manner. In this way, the module maps light duration to a monotonically increasing L_i concentration over the operating window.

To perform temporal filtering of RNA inputs, we designed a dissipative filtering module comprising threshold duplex L_fL_f' and RNase H (Fig. 1b, panel II). In this design, L_fL_f' functions not simply as a reversible reservoir for downstream-active DNA signal strand L_f, but also as a kinetic gate that renders downstream signal transmission dependent on RNA input persistence. Mechanistically, rI invades L_fL_f' to form RNA-DNA hybrid rIL_f', thereby releasing L_f. RNase H then selectively cleaves rI within rIL_f', liberating L_f' that recaptures L_f and restores L_fL_f'. Together, these reactions establish a release-cleavage-recapture cycle that imposes an effective persistence threshold. This threshold is governed by the kinetic balance between input-driven L_f release and input-dissipation-driven L_f recapture: RNA inputs must persist long enough to sustain L_f availability against recapture and enable downstream decision-making. Consequently, transient inputs are attenuated, whereas persistent inputs are transmitted. The filtering stringency can be programmed by varying the L_fL_f' concentration. At a fixed rI input, L_fL_f' with a high concentration promotes faster input consumption and gate resetting, thereby restricting released L_f to a transient pulse. By contrast, L_fL_f' with a low concentration slows resetting and prolongs L_f availability, providing a broader temporal window for downstream decision-making. Thus, L_fL_f' concentration tunes the input requirement for productive signal transmission.

DNA signals generated from the above transduction layer are then fed into a common TIFFN-based decision-making layer. This layer resolves duration-dependent DNA trajectories into discrete decision states through two coupled operations: sequential thresholding and incoherent competitive resolution (Fig. 1b, panel III). Specifically, as the DNA signal crosses programmed thresholds, it engages thresholding duplexes in sequence, thereby releasing ordered, state-defining species. These species enter competing strand-displacement pathways, in which later-arising species displace earlier provisional-state complexes, thereby suppressing the previously accessible states. Through this ordered threshold release and competitive replacement, durations are transformed into mutually exclusive molecular decision states. By varying the arrangement of thresholding duplexes and competitive displacement pathways, this layer can be programmed to tune the onset timing, accessibility window and resolution hierarchy of the resulting states.

To demonstrate the programmability of TIFFN-mediated trajectory-to-state mappings, we designed a set of representative TIFFN topologies that differ in the number and position of programmed thresholds and in the hierarchy of competitive strand-displacement pathways (Fig. 1b, panel IV). Although all TIFFN topologies operate under the same trajectory-to-state decoding principle, these topological parameters reprogram the transfer function, thereby determining how continuous molecular trajectories are partitioned into discrete biochemical decision states. This programmability enables the decoder to generate duration-windowed activation, duration-windowed repression, and duration-dependent ordered multistate progression. Within each decoding mode, systematic tuning of threshold identity and stoichiometry further enables programmable control over response-window location and size. Collectively, these examples establish the TIFFN as a programmable decision-making module where the trajectory-to-state mapping can be systematically reprogrammed.

After decoding, these decoded molecular decisions are coupled to distinct biochemical functions in the actuation layer. This coupling functions as a chemically addressable interface that links decoded decision states to transcriptional, translational, or membrane-level actuation pathways. For transcriptional actuation (Fig. 1b, panel V), selected decision-state complexes are assigned to promoter-activation or promoter-repression functions that regulate the assembly state of nicked T7 promoters,[40,53] thereby directing transcriptional programs. Activation-state complexes assemble transcriptionally competent promoters to initiate RNA synthesis, whereas competing higher-priority decision states terminate the ongoing transcriptional program. The simultaneously assembling cognate promoters initiate the subsequent transcriptional program. Thus, the transcriptional actuation layer provides a programmable decision-to-transcription interface, through which decoded decision states are translated into defined RNA-output programs.

To link transcriptional decoding to translation (Fig. 1b, panel VI), transcriptionally generated RNA outputs function as sequence-specific translational regulators that selectively activate their cognate riboswitch-controlled mRNAs. In this way, each decoded decision state specifies a corresponding protein-expression program, enabling temporal molecular decisions to be propagated from transcription to protein synthesis. To further couple programmable protein expression to membrane-level actuation (Fig. 1b, panel VII), we employed protein α-HL[54,55] as a downstream effector. Duration-gated α-HL synthesis enables transmembrane pore formation and cargo release within the programmed input-duration window. Together, these actuation modules establish a hierarchical decision-to-function cascade, which translates decoded decision states into transcription, translation and membrane-level outputs, ultimately generating functional differentiation in synthetic cells.

Decoding stimulus duration into discrete transcriptional states

To investigate whether stimulus duration could be transduced into DNA trajectories and subsequently resolved into programmable RNA-output states, we implemented the programmable duration-decoding framework at the transcriptional level. We constructed photochemical-integration programmable duration-decoding systems (piPDDSs) that couple photochemical integration, TIFFN-mediated decision-making and transcriptional actuation to decode light duration into discrete transcriptional states (Fig. 2a and Supplementary Section 2). In the photochemical integration module, light duration is converted into DNA signal L_i via the photocleavage of PC linkers embedded in duplex L_iL_i'. Progressive fragmentation of L_i' destabilises L_iL_i', thereby releasing L_i with a concentration trajectory that increases with light duration (Fig. 1b, panel I).

To quantify L_i release as a function of light duration, we employed a fluorophore-quencher reporter, F_1Q_1, whose fluorescence is restored upon L_i-driven strand displacement of F_1. By calibrating fluorescence intensities against known L_i concentrations (Supplementary Fig. 1), we converted the fluorescence signals measured under different light durations into corresponding L_i concentrations (Supplementary Fig. 2). L_i accumulated approximately linearly over 8.0 min, establishing a calibrated duration-to-signal transfer regime for light duration. This regime enables the quantification of L_i trajectory for subsequent TIFFN-mediated decision-making.

We next established the L_i-to-RNA transfer function that defines how L_i concentrations are resolved into programmable RNA-output states by integrating TIFFN-mediated state resolution and transcriptional actuation. To independently characterise this transfer function, we bypassed photochemical L_i generation and directly supplied defined L_i concentrations to TIFFN-I, TIFFN-II, and TIFFN-III (Supplementary Figs. 3a, 4a, and 5a, and Supplementary Section 3). Each TIFFN was integrated with a matched transcriptional actuation module, enabling L_i-dependent state selection to control RNA production. The resulting RNA products, rP_1, rP_2, and rP_3, were quantified by strand displacement with their respective fluorophore-quencher reporters (F_2Q_2 for rP_1, F_3Q_3 for rP_2, and F_4Q_4 for rP_3). These characterisations established quantitative L_i-to-RNA transfer functions that identified the L_i concentration windows for selectively producing RNA outputs. Specifically, TIFFN-I produced a bounded rP_1 activation window, TIFFN-II yielded a bounded rP_1 repression window, and TIFFN-III produced an ordered progression of mutually exclusive RNA-output states (Supplementary Figs. 3b–e, 4b–f, and 5b–g). Using TIFFN-I and TIFFN-II as examples, we further demonstrated programmable control over the response-window location and size by tuning the identity and stoichiometry of threshold species, respectively (Supplementary Figs. 6–9). Together, these L_i-to-RNA transfer functions provide the basis for selecting strand sequences, threshold stoichiometries and transcriptional reaction conditions, enabling the complete piPDDSs to decode light duration into the desired transcriptional output states.

Using the calibrated transfer maps, we assembled complete piPDDSs (Fig. 2a). To determine whether light duration could be converted into a bounded transcriptional activation window, we first constructed the TIFFN-I-mediated system, termed piPDDS-I (Fig. 2b and Supplementary Fig. 10a). In this system, illumination generates a monotonically increasing L_i trajectory, which is then resolved by TIFFN-I with A_1A_1' and B_1B_1' setting the low and high L_i-response thresholds, respectively. As illumination continues, accumulated L_i sequentially crosses these thresholds, releasing A_1 in the short-duration regime and B_1 under prolonged illumination. At short durations, released A_1 forms a decision-state complex, A_1D, which engages transcriptional module T_1 to assemble A_1DT_1, a transcriptionally active template for rP_1 transcription. Upon prolonged illumination, the released B_1 initiates a competing repression-redirection pathway. B_1 displaces A_1 from A_1DT_1, thereby dismantling the rP_1-active state while forming a higher-priority decision-state complex, B_1D. Then, B_1D engages transcriptional module T_2 to assemble B_1DT_2, redirecting transcription to rP_2. Consequently, piPDDS-I was designed to translate light duration into a bounded rP_1 transcriptional response (OFF→ON→OFF), with prolonged illumination redirected to rP_2 transcription. Consistent with this design, neither rP_1 nor rP_2 transcription was detected in the absence of illumination, indicating minimal formation of the corresponding transcriptionally active complexes, A_1DT_1 and B_1DT_2 (Fig. 2c and Supplementary Fig. 10b–d). Illumination within short durations (<3.0 min) selectively induced rP_1 transcription, consistent with A_1D-mediated assembly of A_1DT_1. Illumination exceeding 2.2 min shifted the system toward B_1D-mediated assembly of B_1DT_2, suppressing rP_1 transcription and initiating rP_2 transcription. Together, these results demonstrate that piPDDS-I translates light duration into a bounded transcriptional activation window, confining rP_1 transcription to short durations while routing prolonged illumination to rP_2 output.

Next, to investigate whether the above activation window could be transitioned into a repression window, we replaced TIFFN-I with TIFFN-II while retaining the same input-transduction module, yielding piPDDS-II (Fig. 2d and Supplementary Fig. 11a). In this system, preformed A_1D engages transcriptional module T_1 to assemble A_1DT_1, thereby presetting the system in an rP_1-

ON state. A single-stranded sink, B_2', sets an initial, non-productive L_i threshold, whereas threshold duplexes B_1B_2' and C_1C_2' define the subsequent productive thresholds for the release of B_1 and C_1, respectively. At short light durations, initially generated L_i is captured by B_2', thus A_1DT_1 remains unchallenged and sustains rP_1 transcription. Once this initial sink is saturated, additional L_i sequentially displaces B_1 from B_1B_2' at intermediate durations and C_1 from C_1C_2' under prolonged illumination. At intermediate durations, the released B_1 displaces A_1 from A_1DT_1 to form B_1D, thereby switching off the initially active rP_1 transcription while assembling B_1DT_2 to activate rP_2 transcription. At long durations, the generated C_1 displaces B_1 from B_1DT_2 to form a higher-priority complex, C_1D, thereby switching off rP_2 transcription and assembling C_1DT_3 to restore rP_1 transcription. Together, these sequential state transitions yield an rP_1 ON→OFF→ON response with increasing light duration. Consistent with this design, rP_1 transcription remained active while rP_2 transcription remained inactive during short durations (<1.6 min), indicating that A_1DT_1 predominated (Fig. 2e and Supplementary Fig. 11b–e). At intermediate durations (1.6–4.7 min), the transcriptional output was redirected from rP_1 to rP_2, consistent with the replacement of A_1DT_1 by B_1DT_2. At long durations (>4.7 min), rP_2 transcription was terminated, and rP_1 was restored, in accordance with the substitution of B_1DT_2 by rP_1-active C_1DT_3. This ON→OFF→ON behaviour of rP_1 transcription demonstrates that reprogramming the TIFFN topology from TIFFN-I to TIFFN-II transitions decoding logic from a bounded activation window to a bounded repression window.

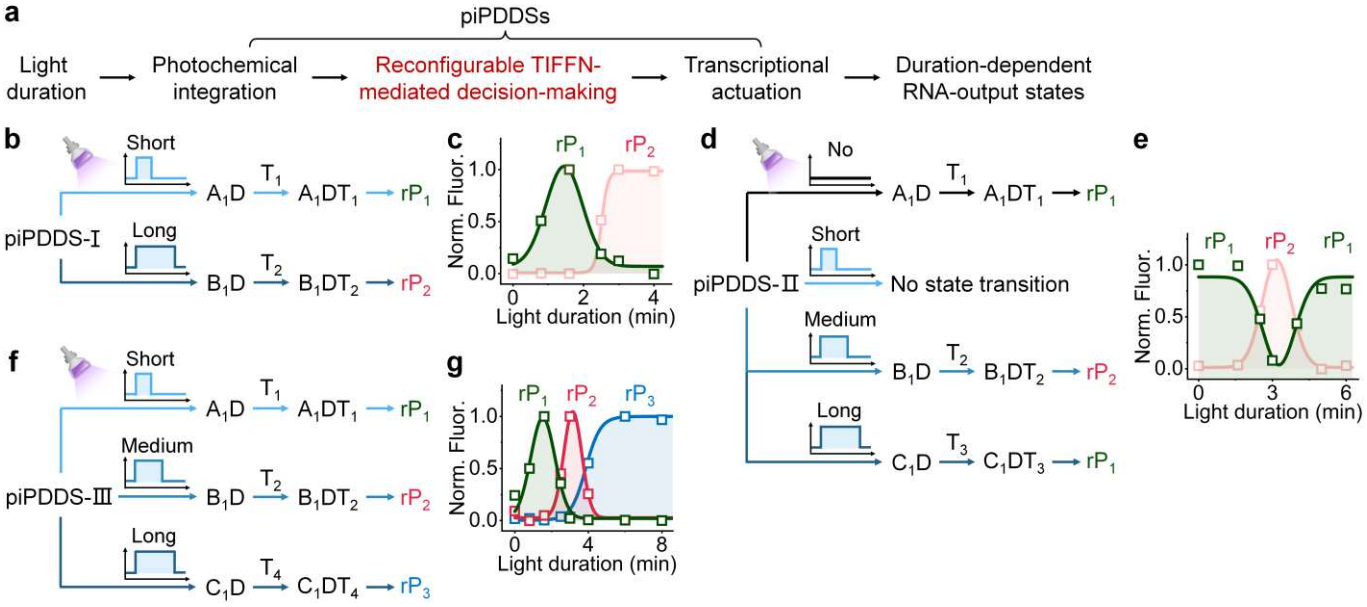


Fig. 2 | Topology-programmed piPDDSs for decoding light duration into distinct transcriptional response landscapes. a, Flowchart showing the operation of piPDDSs, which transform light duration into discrete transcriptional states through sequential photochemical integration, reconfigurable TIFFN-mediated decision-making, and downstream transcriptional actuation. **b**, Schematic illustrating duration-windowed activation of rP_1 transcription dictated by piPDDS-I. **c**, Corresponding normalised fluorescence responses associated with rP_1 and rP_2 transcription derived from Supplementary Fig. 10b–d. **d**, Schematic showing duration-windowed repression of rP_1 transcription governed by piPDDS-II. **e**, Corresponding normalised fluorescence responses associated with rP_1 and rP_2 transcription derived from Supplementary Fig. 11b–e. **f**, Schematic illustrating duration-dependent multistate transcription mediated by piPDDS-III. **g**, Corresponding normalized fluorescence responses associated with rP_1, rP_2, and rP_3 transcription derived from Supplementary Fig. 12b–f.

To further extend duration decoding for multiple output states, we rewired the TIFFN topology to TIFFN-III, generating piPDDS-III, which produces an ordered progression of RNA-output states with increasing light duration. TIFFN-III incorporates three thresholding duplexes, A_1A_1', B_1B_1', and C_1C_1', which establish low, intermediate, and high L_i-response thresholds, respectively. As illumination continues, photochemically accumulated L_i sequentially crosses these thresholds, releasing A_1, B_1, and C_1, which then enter a hierarchical incoherent competitive network (Fig. 2f and Supplementary Fig. 12a). Specifically, A_1 first forms A_1D, which engages transcriptional module T_1 to assemble A_1DT_1 for rP_1 transcription. Later-released B_1 displaces A_1 from A_1DT_1 to form the higher-priority complex B_1D, which engages transcriptional module T_2 to assemble B_1DT_2, redirecting transcription from rP_1 to rP_2. Finally, the last-released C_1 displaces B_1 from B_1DT_2 to form the highest-priority complex, C_1D, which engages transcriptional module T_4 to assemble C_1DT_4 and shift transcription from rP_2 to rP_3. In this way, piPDDS-III implements a stepwise multistate duration decoding. As anticipated, no RNA output was detected in the absence of

illumination. As illumination duration increased, the dominant transcriptional outputs progressed sequentially from rP_1 to rP_2 and then to rP_3 within their respective duration regimes (<3.3 min, 1.8–4.2 min, and >2.5 min, respectively; Fig. 2g and Supplementary Fig. 12b–f). Together, these results demonstrate that piPDDS-III extends duration decoding beyond bounded windows, partitioning a continuous duration axis into a sequential progression of RNA outputs ($rP_1 \rightarrow rP_2 \rightarrow rP_3$).

Collectively, these results show that illumination-duration decoding depends on the integration of photochemical input transduction with TIFFN-mediated decision-making. By altering the TIFFN architecture, the response to the same light-duration input can be programmed as a bounded activation window, a bounded repression window, or an ordered multistate progression of RNA outputs.

Having established that the TIFFN topology supports programmable decoding of light duration, we next asked whether the input-transduction module could be reconfigured while preserving the same downstream architecture. To this end, we replaced photochemical temporal integration with a dissipative RNA-input filtering module and developed a dissipative-filtering programmable duration-decoding system (dfPDDS-I; Fig. 3a, Supplementary Figs. 13 and 14, and Supplementary Section 2). In this architecture, the dissipative-filtering module transduces RNA-input persistence into programmable L_f trajectories that are then resolved by TIFFN-I. Thus, the duration decoding was extended from optical stimuli to molecular RNA signals without altering the downstream architecture. The L_fL_f' reservoir functions as the programmable control element of the dissipative-filtering layer (Fig. 3b). RNA input drives L_f release from the reservoir, whereas RNase H-mediated input dissipation promotes L_f recapture. The dynamic balance between these two processes transduces RNA-input persistence into L_f trajectories with different amplitude and persistence. By varying the reservoir size, this persistence-to-L_f transfer function can be shifted to impose different transmission thresholds. Specifically, a small reservoir establishes a low-persistence threshold, permitting low-level RNA inputs to generate transmissible L_f trajectories, whereas a large reservoir imposes a high-persistence threshold, requiring high-level RNA inputs to produce downstream-activatable L_f trajectories. Regardless of reservoir size, transmitted L_f trajectories are resolved by TIFFN-I, in which A_1A_1' and B_1B_1' define the low and high L_f-response thresholds, respectively. Within the small-reservoir configuration, transmitted L_f trajectories with low amplitudes are designed to reach the low threshold, activating the A_1DT_5 pathway to produce rP_5. By contrast, the high-amplitude trajectories generated within the large-reservoir configuration exceed both thresholds, preferentially engaging the higher-priority B_1DT_6 pathway to generate rP_6. Since RNase H-mediated input dissipation continuously drives L_f recapture, the downstream transcriptional state is maintained only when the transmitted L_f trajectory persists. Therefore, L_f amplitude determines which transcriptional state is selected, whereas L_f persistence defines how long the selected state remains active.

We characterised the dissipative-filtering module independently to determine how reservoir programming shapes the amplitude and persistence of the L_f trajectory before evaluating the complete dfPDDS-I (Fig. 3c–e). We varied the initial rI concentration under each reservoir condition and monitored free L_f using the fluorophore-quencher reporter, F_1Q_1. Reporter fluorescence intensities (Supplementary Fig. 15) were converted into quantitative L_f concentration trajectories using a calibration curve generated from known L_f concentrations (Supplementary Fig. 16). Across the rI concentration assays, higher initial rI concentrations prolonged the effective persistence of the RNA input, resulting in longer-lived L_f trajectories under both reservoir conditions. However, their amplitude and lifetime depended strongly on reservoir size. Under comparable rI ranges, the small L_fL_f' reservoir (0.10 μM) generated low-amplitude but long-lived L_f trajectories (Fig. 3c), whereas the large reservoir (0.63 μM) produced high-amplitude but short-lived trajectories (Fig. 3d). Quantitative analysis of these trajectories revealed a reservoir-dependent trade-off between amplitude and persistence (Fig. 3e), consistent with that reservoir size determines the releasable L_f pool and the kinetics of L_f recapture. Consequently, reservoir programming determines how RNA-input persistence is transduced into L_f trajectories with distinct amplitudes and lifetimes.

To determine how reservoir-programmed L_f trajectories are translated into transcriptional outputs, we assembled complete dfPDDS-I using both the small and large L_fL_f' reservoirs and monitored rP_5 and rP_6 transcription through their ligand-binding-induced fluorescence signals (Fig. 3f–i). Under the small-reservoir configuration, rI at low initial concentrations (<0.20 μM) provided insufficient input persistence, producing only transient L_f trajectories that failed to activate the downstream TIFFN (Fig. 3f and blue squares in the grey-shaded region in Fig. 3j). At initial rI concentration of 0.50 μM or higher, enhanced input persistence enabled L_f trajectories to persist beyond the persistence threshold and activate the low-threshold transcriptional pathway for producing rP_5 (Fig. 3f and blue squares in the green-shaded region in Fig. 3j). Importantly, rP_6 remained negligible throughout the tested rI concentration range (Fig. 3g and blue squares in the grey-shaded region in Fig. 3k), indicating that

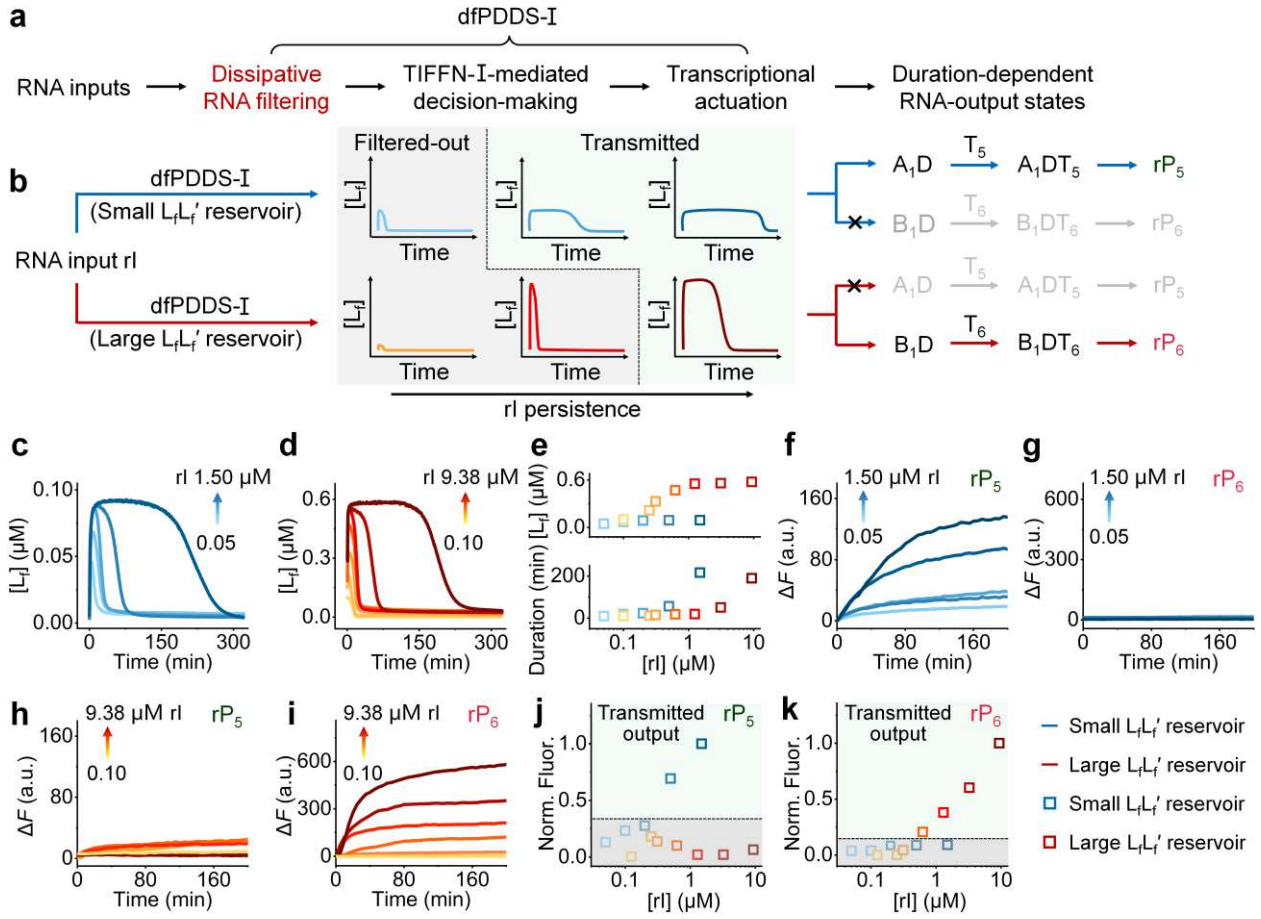


Fig. 3 | Reservoir-programmed dfPDDS-I for converting RNA-input persistence into distinct RNA-output states. a, Flowchart showing the operation of dfPDDS-I, which transforms RNA-input persistence into distinct RNA-output states through sequential dissipative RNA filtering, TIFFN-I-mediated decision-making, and transcriptional actuation. **b**, Schematic illustrating conversion of RNA-input persistence into RNA-output states dictated by dfPDDS-I with small and large L_fL_f' reservoirs. For both L_fL_f' reservoirs, transient rI inputs are dissipatively rejected, whereas sufficiently persistent inputs generate sustained L_f trajectories that exceed the activation threshold of downstream reactions. For persistent inputs, the small L_fL_f' reservoir (blue) generates a low-amplitude L_f trajectory that selectively activates the A_1DT_5 pathway, resulting in rP_5 transcription. In contrast, the large L_fL_f' reservoir (red) generates a high-amplitude L_f trajectory that preferentially activates the orthogonal B_1DT_6 pathway while suppressing A_1DT_5, thereby redirecting the RNA output toward rP_6. **c**,**d**, Time-dependent concentration changes of L_f generated using the small (**c**) and large (**d**) L_fL_f' reservoirs under various rI concentrations, derived from Supplementary Fig. 15a,b, respectively, using the respective calibration curve in Supplementary Fig. 16. **e**, Amplitude (top) and persistence (bottom) of L_f trajectories generated using the small and large reservoirs as a function of rI concentration, derived from **c** and **d**. **f**–**i**, Time-dependent fluorescence changes associated with rP_5 (**f**, **h**) and rP_6 (**g**, **i**) generated using the small (**f**, **g**) and large (**h**, **i**) L_fL_f' reservoirs under various rI concentrations. **j**,**k**, Normalised fluorescence responses associated with rP_5 (**j**) and rP_6 (**k**) as a function of rI concentration, derived from **f** and **h**, as well as from **g** and **i**, respectively. Dashed lines denote the experimentally defined transmission thresholds separating filtered-out and transmitted output states. Green- and grey-shaded regions represent transmitted and filtered-out outputs, respectively.

although the transmitted trajectories satisfied the persistence requirement for signal transmission, their amplitudes remained below the B_1B_1' response threshold required for rP_6 transcription. Thus, the small L_fL_f' reservoir establishes a permissive persistence-selective dissipative-filtering regime that allows relatively low-concentration RNA inputs to pass the dissipative filter, while constraining the transmitted L_f amplitude to the low-threshold rP_5 state. Under the large-reservoir configuration, rI at low initial concentrations (<0.31 μM) produced insufficient input persistence, generating only transient L_f trajectories that were rapidly recaptured before appreciable transcription could occur (Fig. 3i and red squares in the grey-shaded region in Fig. 3k). At initial rI concentration of 0.63 μM or higher, the corresponding increase in effective input persistence enabled L_f trajectories to pass the dissipative filtering to activate the downstream TIFFN. The large L_fL_f' reservoir generated high-amplitude transmitted trajectories that crossed both the low and high response thresholds, thereby preferentially activating the higher-priority B_1DT_6 pathway. Consequently, robust rP_6 transcription was observed (Fig. 3i and red squares in the green-shaded region in Fig. 3k), whereas rP_5 remained negligible throughout the examined rI concentration range (Fig. 3h and red squares in the grey-

shaded region in Fig. 3j). Therefore, the large L_fL_f' reservoir establishes a more stringent dissipative-filtering regime, restricting transmission to higher-concentration RNA inputs, while generating transmitted L_f trajectories with their amplitudes sufficient to cross the high response threshold and selectively activate the rP_6-producing pathway.

Comparison of the normalized input-output maps shows that reservoir programming reconfigures dissipative RNA filtering by shifting the persistence requirement for signal transmission. Although the initial rI concentration was varied experimentally, whether an input is transmitted is determined not by its instantaneous abundance alone, but by whether it persists long enough to sustain a downstream-active L_f signal. Together, these results establish persistence-gated signal transmission, in which temporal persistence of an input determines whether it is propagated to the downstream decision-making layer.

Duration decoding programs distinct RNA-output states in synthetic cells

We next examined whether the duration-decoding logic established in bulk solution could be transferred to synthetic-cell compartments. To do so, we encapsulated the piPDDSs in giant unilamellar vesicles (GUVs). Before evaluating duration decoding, we first assessed the operability of each layer after compartmentalisation. For the temporal input transduction layer, Supplementary Fig. 17 shows that L_i accumulated in a duration-dependent manner, confirming light-duration integration within GUVs. Next, we investigated the downstream decision-making and transcriptional actuation layers by monitoring RNA production through strand displacement with corresponding fluorophore-quencher reporters. Single-vesicle fluorescence imaging results and population-averaged response analyses (Supplementary Figs. 18−20) demonstrate that these layers remained functional after compartmentalisation (Supplementary Section 3).

We then investigated whether synthetic cells containing the complete piPDDSs could convert light duration into programmable transcriptional states. Single-vesicle fluorescence images revealed distinct duration-dependent output patterns across these three piPDDS architectures (Fig. 4a–e), which were further quantified by population-averaged duration-response analyses (Fig. 4f–j). In piPDDS-I synthetic cells (Fig. 4a,f and Supplementary Fig. 21), negligible reporter fluorescence was observed without illumination, consistent with the lack of photochemical L_i release and minimal formation of transcriptionally active complexes. Upon illumination, rP_1-associated reporter fluorescence appeared within an intermediate duration window (0.5–2.4 min), whereas prolonged illumination produced rP_2-associated reporter fluorescence (>1.6 min). Having established an activation window for rP_1 transcription in GUVs, we next tested whether its location and size could be programmed independently. Introducing an additional A_1' threshold shifted the rP_1 activation window from 0.5–2.4 min to 1.3–6.1 min (Fig. 4b,g and Supplementary Fig. 22). However, increasing the fraction of A_1A_1' threshold broadened the response-window size from 0.5–2.4 min to 0.1–6.0 min (Fig. 4c,h and Supplementary Fig. 23). Together, these results demonstrate that synthetic cells can be programmed to decode light duration into a bounded transcriptional activation window with tunable temporal boundaries. We next explored whether reconfiguring the network topology could generate distinct duration-decoding behaviours. In piPDDS-II synthetic cells (Fig. 4d,i and Supplementary Fig. 24), rP_1 dominated under short illumination (<1.6 min), whereas rP_2 output remained low, indicating that rP_1 transcription was initially active. Within the intermediate window (1.6–4.7 min), the transcriptional output shifted from rP_2 to rP_1. At long durations (>4.7 min), rP_1 output reemerged while rP_2 output disappeared, indicating the restoration of rP_1 transcription. Thus, piPDDS-II synthetic cells decoded light duration into a bounded repression window for rP_1 transcription. Further reconfiguration to piPDDS-III produced a multistate response in synthetic cells (Fig. 4e,j and Supplementary Fig. 25). At short durations (0–3.1 min), rP_1 was the predominant output. At intermediate durations (1.8–4.2 min), rP_2 output became dominant as rP_1 output decreased. At long durations (>3.0 min), rP_3 output became predominant as rP_1 and rP_2 outputs diminished. These transitions yielded an ordered $rP_1 \rightarrow rP_2 \rightarrow rP_3$ progression with increasing light durations in synthetic cells.

Although compartmentalisation into GUVs broadened vesicle-to-vesicle fluorescence heterogeneity relative to bulk solution, population-averaged duration-response analysis (Fig. 4f–j) confirmed that the programmed RNA-output response profiles are faithfully preserved in synthetic cells. Together, these results demonstrate that light duration can serve as a programmable temporal input for specifying transcriptional response landscapes of synthetic cells, including windowed activation, windowed repression, ordered multistate progression, and tunable response-window location and size.

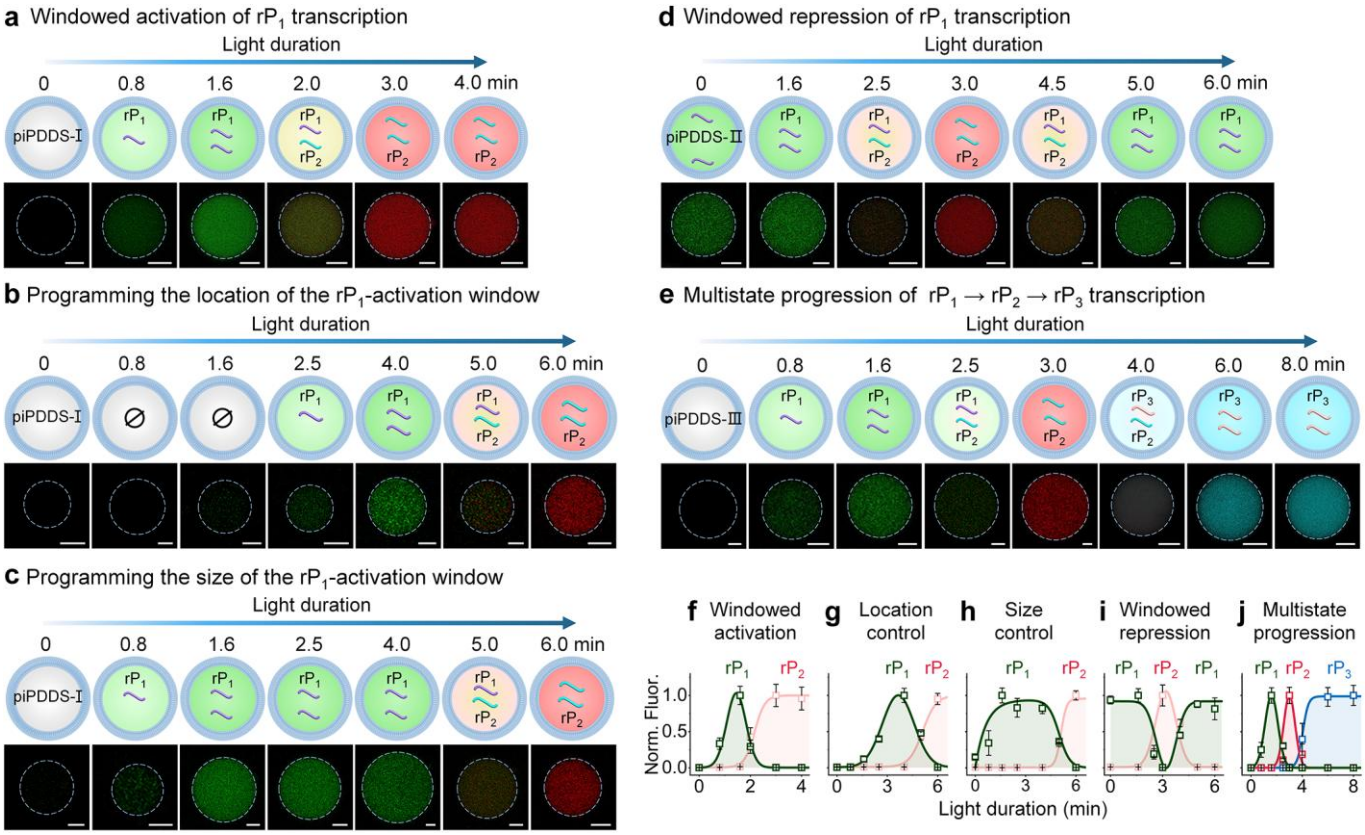


Fig. 4 | Light-duration decoding programmed transcriptional state differentiation in synthetic cells. a–c, Schematic and representative confocal images depicting duration-windowed activation of rP_1 transcription in piPDDS-I synthetic cells (**a**) and programmable tuning the location (**a**) and size (**b**) of the rP_1-activation window. For **b** and **c**, piPDDS-I was supplemented with 0.16 μM A_1' and 0.16 μM A_1A_1', respectively. **d**, Schematic and representative confocal images depicting duration-windowed repression of rP_1 transcription in piPDDS-II synthetic cells. **e**, Schematic and representative confocal images showing duration-dependent multistate transcription in piPDDS-III synthetic cells. **f–j**, Corresponding statistical analyses of normalised fluorescence responses associated with RNA outputs as a function of light duration for windowed rP_1 activation (**f**), programmable shifts in location (**g**) and size (**h**) of the rP_1-activation window, windowed rP_1 repression (**i**), and multistate transcriptional progression (**j**). Scale bars, 5 μm. Green, red, and blue in confocal images represent fluorescence associated with rP_1, rP_2, and rP_3, respectively. Corresponding individual fluorescence channels of confocal images in **a–e** are depicted in Supplementary Figs. 21–25, respectively. Statistical data in **f–j** are presented as mean ± s.d. of three independent experiments.

Duration decoding drives differential protein synthesis in synthetic cells

Having demonstrated that synthetic cells can decode light duration into discrete transcriptional states, we next investigated whether these RNA states could be propagated across the transcription-translation boundary to produce distinct protein-expression states. To this end, we interfaced three piPDDSs, I–III, with the corresponding riboswitch-controlled translation module,[14,56] enabling duration-dependent RNA outputs to regulate protein synthesis in synthetic cells (Fig. 5a). Accordingly, the resulting synthetic cells were designed to decode light duration into distinct protein-output states.

We first evaluated whether duration-dependent RNA outputs could direct protein synthesis in a bulk cell-free expression system, using time-dependent fluorescent-protein accumulation as the readout (Supplementary Fig. 26a). In the integrated piPDDS-I/riboswitch architecture (Supplementary Fig. 26b–e), rP_1 serves as the RNA trigger to activate the green fluorescent protein (GFP)-regulating riboswitch module, whereas rP_2 lacks riboswitch-activating activity and is translationally inert. In the absence of light, GFP fluorescence remained low. Illumination within the defined duration window (<3.7 min) induced GFP accumulation, consistent with rP_1 production and its triggered translation of GFP. Prolonged illumination (>3.7 min) suppressed GFP synthesis as the piPDDS-I output shifted from rP_1 to rP_2. Thus, the piPDDS-I/riboswitch coupling propagates the duration-dependent rP_1 transcriptional state to the protein level, leading to a corresponding duration window for GFP synthesis.

To extend the protein-expression logic from windowed activation to windowed repression, we integrated piPDDS-II with the same rP_1-responsive GFP-regulating riboswitch module (Supplementary Fig. 27). In this architecture, GFP fluorescence was high at short light durations (<1.6 min), consistent with the dominant rP_1-producing transcriptional state. Within the programmed

repression window (1.6–4.7 min), GFP fluorescence decreased as the piPDDS-II output shifted from rP_1 to rP_2. At long light durations (>4.7 min), GFP production recovered, in accordance with re-entry into the rP_1-producing transcriptional state. Thus, the windowed rP_1 repression state was transmitted to the protein level as a corresponding GFP-repression window. To translate the piPDDS-III-governed RNA-output progression into distinct protein-output states, we assigned rP_1 and rP_2 as the RNA triggers for the GFP- and mCherry-regulating riboswitch modules, respectively, while leaving rP_3 unassigned to generate a protein-silent state (Supplementary Fig. 28). In this architecture, both GFP and mCherry fluorescence remained low in the absence of light. Upon illumination, GFP fluorescence dominated in the short-duration regime (<3.8 min), whereas mCherry fluorescence increased with prolonged illumination and became dominant within the intermediate-duration regime (1.9–5.2 min). Further extension of illumination (>5.2 min) yielded minimal GFP and mCherry fluorescence, consistent with entry into the rP_3-associated protein-silent regime. Thus, the ordered RNA-state progression was propagated across the transcription-translation boundary to generate sequential protein-output states, GFP→mCherry→silent, across successive light-duration regimes.

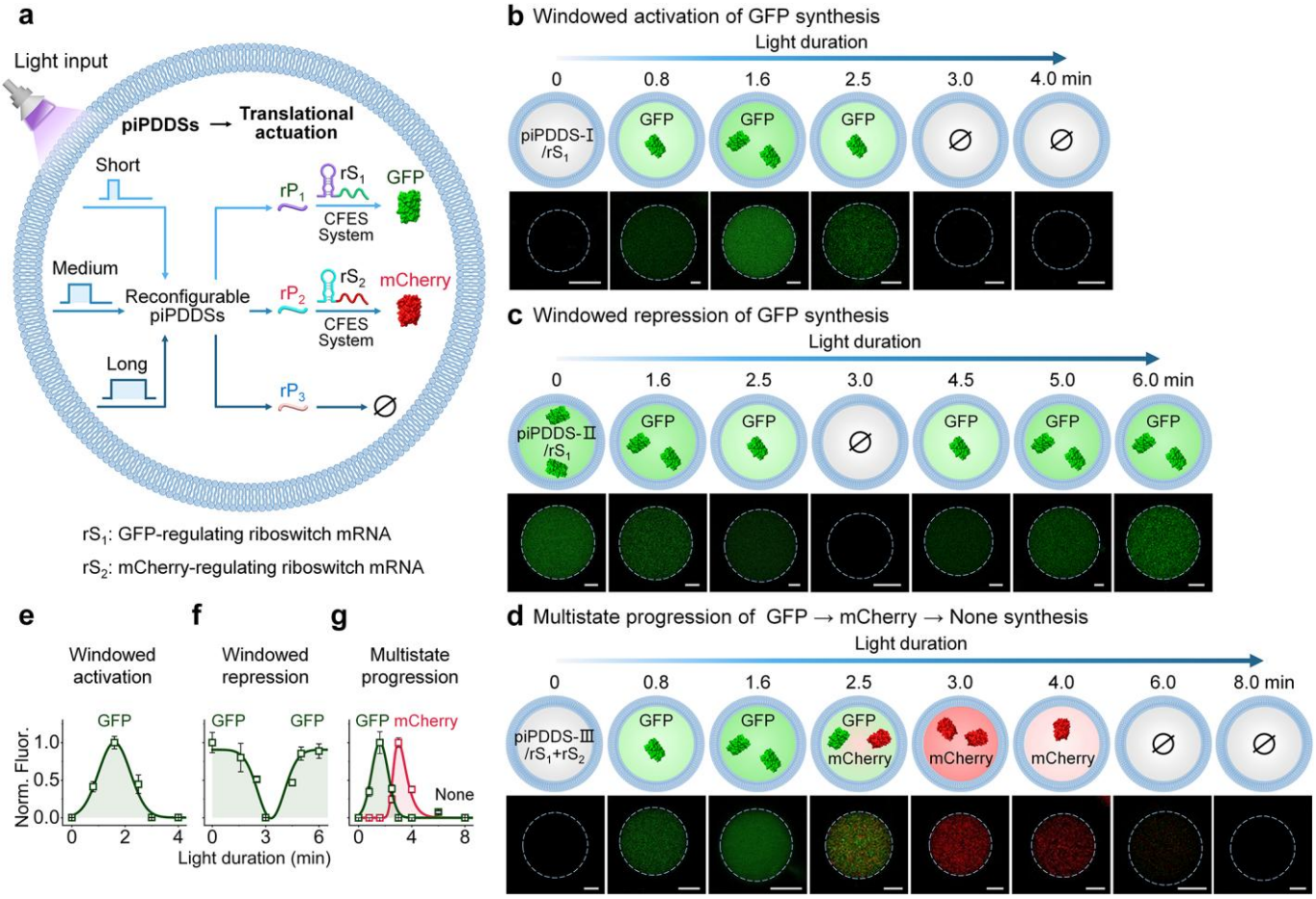


Fig. 5 | Light-duration decoding directed translational state differentiation in synthetic cells. a, Schematic showing light-duration decoding-driven translational actuation dictated by reconfigurable piPDDSs. RNA-output states generated by piPDDSs are coupled to riboswitch-controlled cell-free expression systems (CFESs): rP_1 activates GFP synthesis through the GFP-regulating riboswitch mRNA (rS_1), rP_2 activates mCherry synthesis through the mCherry-regulating riboswitch mRNA (rS_2), and rP_3 specifies a translationally inactive state. **b**, Schematic and representative confocal images showing duration-windowed activation of GFP synthesis in the synthetic cells containing piPDDS-I and an rS_1-controlled CFES. **c**, Schematic and representative confocal images depicting duration-windowed repression of GFP synthesis in synthetic cells containing piPDDS-II and an rS_1-controlled CFES. **d**, Schematic and representative confocal images depicting duration-dependent multistate protein-expression progression in synthetic cells containing piPDDS-III, as well as an rS_1- and rS_2-controlled CFES. **e**–**g**, Corresponding statistical analyses of normalised fluorescence responses of protein outputs as a function of light duration for windowed GFP activation (**e**), windowed GFP repression (**f**), and multistate progression from GFP synthesis to mCherry synthesis and finally to the translationally inactive state (**g**). Scale bars, 5 μm. Green and red in confocal images represent GFP and mCherry fluorescence, respectively. Corresponding individual fluorescence channels of confocal images in **d** are depicted in Supplementary Fig. 29. Statistical data in **e**–**g** are presented as mean ± s.d. of three independent experiments.

We next constructed synthetic cells containing each of these three piPDDS/riboswitch architectures and monitored their duration-dependent protein-expression programs by time-lapse confocal fluorescence imaging of individual vesicles. Population-averaged fluorescence analysis was then used to characterise protein-expression profiles within their corresponding light-duration regimes. In synthetic cells containing the integrated piPDDS-I/riboswitch architecture (Fig. 5b,e), GFP fluorescence was observed within the programmed light-duration window (<3.0 min). Outside this window, vesicles remained in a GFP-low state. Thus, the GFP-ON state is confined to the prescribed light-duration window, demonstrating that synthetic cells can translate light duration into a bounded protein-expression state. In synthetic cells implementing the integrated piPDDS-II/riboswitch program (Fig. 5c,f), GFP fluorescence was high at short light durations (<1.5 min) and markedly reduced within the intermediate light-duration window (1.5–4.6 min). At longer durations (>4.6 min), GFP expression was restored. Together, these responses demonstrate that synthetic cells can decode light duration into a windowed protein-repression state. Finally, synthetic cells containing the integrated piPDDS-III/riboswitch architecture implemented sequential protein-output selection (Fig. 5d,g and Supplementary Fig. 29). Both GFP and mCherry fluorescence remained low in the absence of light. Illumination within the <3.7 min window resulted in GFP-dominant/mCherry-low vesicles, whereas exposure within the 2.1–5.0 min window induced an mCherry-dominant/GFP-low state. Further extension of illumination (>5.0 min) led to GFP-low/mCherry-low vesicles. Collectively, the GFP→mCherry→silent protein-output progression mirrors the upstream $rP_1 \rightarrow rP_2 \rightarrow rP_3$ RNA-state sequence, demonstrating that synthetic cells can convert light duration into distinct and ordered protein-expression states.

Population-averaged fluorescence analyses (Fig. 5e–g) quantified distinct duration-dependent protein-expression profiles across these three synthetic-cell systems, in agreement with the corresponding bulk measurements (Supplementary Figs. 26e, 27d, and 28f). Collectively, these experiments show that synthetic cells can decode light duration directly into programmable protein-expression states. Depending on the embedded duration-decoding logic, the same light input can be mapped onto a duration-windowed activation state, a duration-windowed state, or an ordered multistate progression.

Duration-windowed membrane permeabilisation in synthetic cells

We next extended duration decoding functions from protein-expression control to duration-selective membrane permeabilisation. To implement this function, we co-encapsulated piPDDS-I, an rP_1-gated α-HL-regulating riboswitch module, and Cyanine 5 (Cy5) as a model small-molecule cargo in synthetic cells (Fig. 6a). When synthetic cells are exposed to light durations within the piPDDS-I activation window, the network selects the rP_1 state that activates α-HL translation. The resulting α-HL monomers assemble into heptameric transmembrane pores in the lipid bilayer, thereby switching synthetic cells into a membrane-permeabilising state and enabling Cy5 efflux. Outside this programmed duration window, due to the absence of rP_1 production, α-HL production remains low, thus maintaining membrane integrity and Cy5 retention. Therefore, duration decoding is propagated from molecular state selection to membrane-level function, endowing synthetic cells with a permeabilising state that is constrained within a programmed temporal window.

To assess membrane permeabilisation, we monitored Cy5 efflux from GUVs as a reporter of α-HL-mediated transmembrane transport. We first investigated whether Cy5-loaded GUVs exhibited spontaneous leakage (Fig. 6b and Supplementary Fig. 30). In the absence of α-HL, Cy5 was retained within the vesicles over 2.0 h, confirming negligible nonspecific leakage (Fig. 6c). We then utilised time-lapse confocal fluorescence microscopy to track Cy5 efflux from individual synthetic cells containing the complete piPDDS-I/α-HL riboswitch system and Cy5. Confocal images (Fig. 6d) and population-averaged duration-response profiles (Fig. 6e) show that non-illuminated synthetic cells retained nearly constant intravesicular Cy5 fluorescence over 2.0 h, indicating minimal cargo efflux and an α-HL-OFF membrane state. However, illumination within the duration window (1.6–5.2 min) induced a rapid decrease in intravesicular Cy5 fluorescence, consistent with rP_1-gated α-HL synthesis and consequent cargo release. At prolonged illumination durations beyond this window, Cy5 fluorescence remained stable, consistent with redirection of the piPDDS-I output from rP_1 to the non-activating rP_2 and restoration of a membrane-retentive state. To assess the membrane integrity during the Cy5-release process, we labelled the GUV membrane with a FAM-conjugated cholesterol-modified DNA strand. Membrane-associated FAM fluorescence persisted before and after Cy5 efflux, indicating that GUVs remain structurally intact during cargo release and supporting α-HL-mediated pore transport rather than membrane disruption (Fig. 6b and Supplementary Fig. 30). Together, these results demonstrate that synthetic cells can decode light duration into a duration-windowed membrane-permeabilisation response, thereby restricting cargo release to a programmed range of stimulus durations.

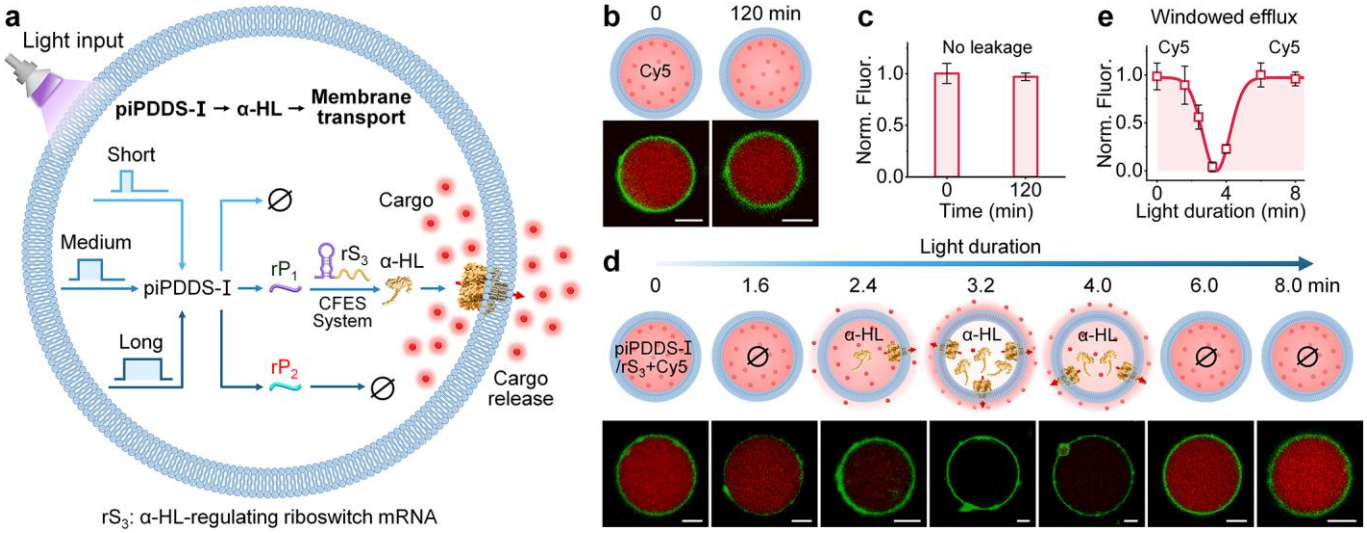


Fig. 6 | Light-duration decoding enabled windowed membrane permeabilisation and cargo release in synthetic cells. **a**, Schematic illustrating duration-dependent membrane permeabilisation in synthetic cells containing piPDDS-I, a CFES controlled by rP_1-gated α-HL-regulating riboswitch (rS_3), and Cyanine 5 (Cy5) as a model small-molecule cargo. Within the programmed activation window, piPDDS-I generates rP_1 that activates α-HL synthesis, leading to pore formation and cargo release. At shorter and longer light durations outside this window, the piPDDS-I outputs do not activate α-HL synthesis, thereby maintaining membrane integrity and cargo retention. **b**, Schematic and representative confocal images of the synthetic cells containing Cy5 cargo and FAM-labelled membrane markers after incubation at 37 °C for 0 and 120 min. **c**, Normalised intravesicular Cy5 fluorescence intensity corresponding to the data in **b**. **d**, Schematic and representative confocal images illustrating duration-windowed cargo release from the synthetic cells containing the integrated piPDDS-I/rS_3 architecture and Cy5. **e**, Corresponding statistical analyses of normalised intravesicular Cy5 fluorescence intensity. Scale bars, 5 µm. Green and red in confocal images represent fluorescence of FAM-labelled membrane and encapsulated Cy5 cargo, respectively. Corresponding individual fluorescence channels of confocal images in **b** and **d** are depicted in Supplementary Figs. 30 and 31, respectively. Statistical data in **e** are presented as mean ± s.d. of three independent experiments.

Conclusion

Stimulus duration poses a distinct challenge for chemical information processing, as it is inherently history-dependent. Decoding it requires chemical systems to transform the temporal evolution of an input into a molecular representation through programmed reaction kinetics. This molecular representation can then be relayed to coupled downstream reaction networks, which process it into discrete decision states for determining the functional output of the system. In this view, duration decoding is not a property of any individual reaction, but an emergent function arising from the coordinated dynamics of an organised reaction network. Here, we establish a programmable duration-decoding framework that implements this principle by integrating temporal input transduction, molecular decision-making and functional actuation. Embedding this framework within synthetic cells endows them with the capacity to transduce stimulus duration into molecular trajectories and subsequently decode these trajectories into discrete molecular states, thereby directing duration-dependent functional differentiation.

The duration-to-trajectory transduction is achieved via two complementary kinetic mechanisms. In the photochemical integration mode, light duration is integrated through progressive accumulation of an active molecular species, mapping elapsed exposure time onto molecular trajectories. In the dissipative filtering mode, duration is transduced through persistence against programmed dissipation, so only sufficiently sustained inputs generate molecular trajectories that reach the downstream decoder. Despite their distinct chemistries, both convert stimulus duration into molecular trajectories, providing a common representation of temporal information. The molecular meaning assigned to such a trajectory is not intrinsic to the trajectory itself, but emerges from the architecture and dynamics of the network that interprets it. Threshold-gated incoherent feedforward networks convert these trajectories into discrete molecular states. Network topology specifies the qualitative decoding logic, including windowed activation, windowed repression, and multistate progression, whereas kinetics and stoichiometry tune the associated decision boundaries, enabling programmable control over the response window's location and size.

Importantly, the decoded states are not merely readouts of temporal information, but can serve as executable states to control synthetic-cell functions. Interfacing these states with transcriptional and translational modules allows decoded molecular

decisions to control RNA and protein synthesis, while coupling them to membrane-active effectors extends this control to membrane-level synthetic-cell behaviours. Thus, otherwise identical synthetic cells can acquire distinct functional states solely according to stimulus duration, extending temporal decoding from molecular decision-making to cell-like behaviour.

Rather than reconstructing a specific biological pathway, this framework abstracts a general organising logic of temporal decoding. In natural systems, duration decoding is often embedded within tightly coupled sensing, regulatory and effector processes, obscuring the underlying information-processing principles and limiting their systematic reconfiguration. Our framework instead resolves this function into three chemical operations and reconstructs their organisation from the bottom up, allowing each operation to be independently programmed and then chemically integrated. Nucleic acid chemistry provides a complementary bottom-up design space for this purpose: sequence-defined molecular recognition establishes network connectivity, while reaction kinetics, stoichiometry, and molecular turnover shape the trajectories, thresholds, and state lifetimes, through which stimulus duration is represented and interpreted. The compatibility of nucleic acids with cell-free transcription and translation allows these molecular decisions to be directly coupled to biochemical functions.

Stimulus duration represents only one dimension of a broader temporal information space that chemical systems could, in principle, decode. Related design principles could be extendable to other temporal features, including frequency and order, by coupling appropriate kinetic architectures with matched molecular decoders. Interfacing these temporal-decoding architectures with diverse functional modules could enable synthetic cells and other adaptive chemical systems to select functions based on the temporal structure of environmental cues. More broadly, this work establishes a programmable chemical route for converting temporal information into executable molecular decisions, expanding chemical information processing from what a signal is and how much is present to how it unfolds over time.

References

1. Buddingh', B. C. & van Hest, J. C. M. Artificial cells: synthetic compartments with life-like functionality and adaptivity. *Acc. Chem. Res.* **50**, 769–777 (2017).
2. Guindani, C., Caire da Silva, L., Cao, S., Ivanov, T. & Landfester, K. Synthetic cells: from simple bio-inspired modules to sophisticated integrated systems. *Angew. Chem. Int. Ed.* **61**, e202110855 (2022).
3. Samanta, A., Baranda Pellejero, L., Masukawa, M. & Walther, A. DNA-empowered synthetic cells as minimalistic life forms. *Nat. Rev. Chem.* **8**, 454–470 (2024).
4. Fletcher, M., Diggines, B. & Elani, Y. Molecular systems engineering of synthetic cells. *Nat. Chem.* **18**, 14–22 (2026).
5. Behar, M. & Hoffmann, A. Understanding the temporal codes of intra-cellular signals. *Curr. Opin. Genet. Dev.* **20**, 684–693 (2010).
6. Purvis, J. E. & Lahav, G. Encoding and decoding cellular information through signaling dynamics. *Cell* **152**, 945–956 (2013).
7. Sonnen, K. F. & Aulehla, A. Dynamic signal encoding—from cells to organisms. *Semin. Cell Dev. Biol.* **34**, 91–98 (2014).
8. Yang, S. & Jin, F. Why the temporal dimension matters in cellular signalling. *Nat. Cell Biol.* **28**, 1599–1605 (2026).
9. Murphy, L. O., Smith, S., Chen, R.-H., Fingar, D. C. & Blenis, J. Molecular interpretation of ERK signal duration by immediate early gene products. *Nat. Cell Biol.* **4**, 556–564 (2002).
10. Dupin, A. & Simmel, F. C. Signalling and differentiation in emulsion-based multi-compartmentalized in vitro gene circuits. *Nat. Chem.* **11**, 32–39 (2019).
11. Joesaar, A. *et al.* DNA-based communication in populations of synthetic protocells. *Nat. Nanotechnol.* **14**, 369–378 (2019).
12. Higashi, S. L. *et al.* Adaptive metal ion transport and metalloregulation-driven differentiation in pluripotent synthetic cells. *Nat. Chem.* **17**, 54–65 (2025).
13. Meng, H. *et al.* Asymmetric splitting in dividing lipid-nucleotide multilamellar droplets. *Nature* **653**, 418–424 (2026).
14. Dwidar, M. *et al.* Programmable artificial cells using histamine-responsive synthetic riboswitch. *J. Am. Chem. Soc.* **141**, 11103–11114 (2019).
15. Liu, S. et al. Enzyme-mediated nitric oxide production in vasoactive erythrocyte membrane-enclosed coacervate protocells. *Nat. Chem.* **12**, 1165–1173 (2020).
16. Fan, S. *et al.* A synthetic cell microreactor with two types of interacting dynamic DNA-based pores. *Nat. Chem*. **18**, 1325–1333 (2026).
17. Smith, J. M., Hartmann, D. & Booth, M. J. Engineering cellular communication between light-activated synthetic cells and

bacteria. *Nat. Chem. Biol.* **19**, 1138–1146 (2023).
18. Zhao, Q.-H., Qi, J.-Y. & Deng, N.-N. DNA photofluids show life-like motion. *Nat. Mater.* **24**, 935–944 (2025).
19. Monck, C., Elani, Y. & Ceroni, F. Genetically programmed synthetic cells for thermo-responsive protein synthesis and cargo release. *Nat. Chem. Biol.* **20**, 1380–1386 (2024).
20. Gerardin, J., Reddy, N. R. & Lim, W. A. The design principles of biochemical timers: circuits that discriminate between transient and sustained stimulation. *Cell Syst.* **9**, 297−308 (2019).
21. Lormeau, C., Rudolf, F. & Stelling, J. A rationally engineered decoder of transient intracellular signals. *Nat. Commun.* **12**, 1886 (2021).
22. Nussinov, R., Zhang, W., Liu, Y. & Jang, H. Mitogen signaling strength and duration can control cell cycle decisions. *Sci. Adv.* **10**, eadm9211 (2024).
23. Song, Y. H., Shim, J. S., Kinmonth-Schultz, H. A. & Imaizumi, T. Photoperiodic flowering: time measurement mechanisms in leaves. *Annu. Rev. Plant Biol.* **66**, 441–464 (2015).
24. Marshall, C. J. Specificity of receptor tyrosine kinase signaling: transient versus sustained extracellular signal-regulated kinase activation. *Cell* **80**, 179–185 (1995).
25. Rosenbloom, A. B. *et al.* β-Catenin signaling dynamics regulate cell fate in differentiating neural stem cells. *Proc. Natl. Acad. Sci. USA* **117**, 28828–28837 (2020).
26. Teague, S. *et al.* Time-integrated BMP signaling determines fate in a stem cell model for early human development. *Nat. Commun.* **15**, 1471 (2024).
27. Meyer, K., Huang, B. & Weiner, O. D. Emerging roles of transcriptional condensates as temporal signal integrators. *Nat. Rev. Genet.* **26**, 559–570 (2025).
28. Litvak, V. *et al.* Function of C/EBPδ in a regulatory circuit that discriminates between transient and persistent TLR4-induced signals. *Nat. Immunol.* **10**, 437–443 (2009).
29. Zechner, C., Seelig, G., Rullan, M. & Khammash, M. Molecular circuits for dynamic noise filtering. *Proc. Natl. Acad. Sci. USA* **113**, 4729–4734 (2016).
30. Santos, S. D. M., Verveer, P. J. & Bastiaens, P. I. H. Growth factor-induced MAPK network topology shapes Erk response determining PC-12 cell fate. *Nat. Cell Biol.* **9**, 324–330 (2007).
31. Purvis, J. E. *et al.* p53 dynamics control cell fate. *Science* **336**, 1440–1444 (2012).
32. Soloveichik, D., Seelig, G. & Winfree, E. DNA as a universal substrate for chemical kinetics. *Proc. Natl. Acad. Sci. USA* 107, 5393–5398 (2010).
33. Del Grosso, E., Franco, E., Prins, L. J. & Ricci, F. Dissipative DNA nanotechnology. *Nat. Chem.* **14**, 600–613 (2022).
34. Wang, X., Wang, S., Yue, L. & Tan, W. Designing generative dissipative networks for programming complex temporal dynamics and functions. *Chem* **11**, 102593 (2025).
35. Jia, S., Lv, H., Li, Q., Fan, C. & Wang, F. DNA-based biocomputing circuits and their biomedical applications. *Nat. Rev. Bioeng.* **3**, 535–548 (2025).
36. Jones, M. R., Seeman, N. C. & Mirkin, C. A. Programmable materials and the nature of the DNA bond. *Science* **347**, 1260901 (2015).
37. Zhang, D. Y. & Winfree, E. Control of DNA strand displacement kinetics using toehold exchange. *J. Am. Chem. Soc.* **131**, 17303–17314 (2009).
38. Zhang, D. Y. & Seelig, G. Dynamic DNA nanotechnology using strand-displacement reactions. *Nat. Chem.* 3, 103–113 (2011).
39. Montagne, K., Gines, G., Fujii, T. & Rondelez, Y. Boosting functionality of synthetic DNA circuits with tailored deactivation. *Nat. Commun.* **7**, 13474 (2016).
40. Schaffter, S. W. & Schulman, R. Building in vitro transcriptional regulatory networks by successively integrating multiple functional circuit modules. *Nat. Chem.* **11**, 829–838 (2019).
41. Zhong, R. *et al.* Continuously tunable multistability in DNA replication networks. *Nat. Commun.* **17**, 1782 (2026).
42. Lv, H. *et al.* DNA-based programmable gate arrays for general-purpose DNA computing. *Nature* **622**, 292–300 (2023).
43. Song, T. & Qian, L. Heat-rechargeable computation in DNA logic circuits and neural networks. *Nature* **646**, 315–322 (2025).
44. Srinivas, N., Parkin, J., Seelig, G., Winfree, E. & Soloveichik, D. Enzyme-free nucleic acid dynamical systems. *Science* **358**, eaal2052 (2017).

45. Machinek, R. R. F., Ouldridge, T. E., Haley, N. E. C., Bath, J. & Turberfield, A. J. Programmable energy landscapes for kinetic control of DNA strand displacement. *Nat. Commun.* **5**, 5324 (2014).
46. Bucci, J., Irmisch, P., Del Grosso, E., Seidel, R. & Ricci, F. Orthogonal enzyme-driven timers for DNA strand displacement reactions. *J. Am. Chem. Soc.* **144**, 19791–19798 (2022).
47. Song, T. *et al.* Fast and compact DNA logic circuits based on single-stranded gates using strand-displacing polymerase. *Nat. Nanotechnol.* **14**, 1075–1081 (2019).
48. Chen, S., Shu, W., Wang, S., Yue, L. & Tan, W. Bioinspired nucleic acid-based bandpass filters and their concentration-adaptive functions. *J. Am. Chem. Soc.* **147**, 12786–12799 (2025).
49. Do, S., Lee, C., Lee, T., Kim, D.-N. & Shin, Y. Engineering DNA-based synthetic condensates with programmable material properties, compositions, and functionalities. *Sci. Adv.* **8**, eabj1771 (2022).
50. Dong, J. & Willner, I. Synthetic dynamic transcription frameworks and their applications. *Nat. Chem.* **18**, 227–245 (2026).
51. Ordoukhanian, P. & Taylor, J.-S. Design and synthesis of a versatile photocleavable DNA building block. Application to phototriggered hybridization. *J. Am. Chem. Soc.* **117**, 9570–9571 (1995).
52. Huang, F. *et al.* Light-responsive and pH-responsive DNA microcapsules for controlled release of loads. *J. Am. Chem. Soc.* **138**, 8936–8945 (2016).
53. Kim, J., White, K. S. & Winfree, E. Construction of an in vitro bistable circuit from synthetic transcriptional switches. *Mol. Syst. Biol.* **2**, MSB4100099 (2006).
54. Song, L. *et al.* Structure of staphylococcal α-hemolysin, a heptameric transmembrane pore. *Science* **274**, 1859–1866 (1996).
55. Parkes, E. *et al.* Magnetic activation of spherical nucleic acids enables the remote control of synthetic cells. *Nat. Chem.* **17**, 1505–1513 (2025).
56. Pardee, K. *et al.* Paper-based synthetic gene networks. *Cell* **159**, 940–954 (2014).

Methods

Preparation of giant unilamellar vesicles (GUVs). A lipid-in-oil phase was prepared by mixing POPC (450 μg) and cholesterol (50 μg) in 2 mL of chloroform, followed by rotary evaporation to form a thin film. The film was resuspended in 2 mL of mineral oil and incubated at 80 °C for 30 min to ensure homogeneity. The resulting solution was aliquoted and stored at 4 °C overnight. An inner aqueous solution containing 300 mM sucrose, 10 mM Mg^{2+} and a specific network system was prepared, while an outer aqueous solution consisted of 300 mM glucose and 10 mM Mg^{2+}. GUVs were generated using a water-in-oil emulsion transfer method. Briefly, 10 μL of the inner solution was emulsified in 200 μL of the lipid-in-oil phase by pipette mixing, and then this emulsion was layered over 100 μL of the outer aqueous solution. After equilibration at 4 °C for 1.5 h and centrifugation (4,000 × g, 10 min), the GUV pellets were harvested and resuspended in 20 μL of the outer solution.

Probing light-duration decoding programmed distinct RNA-output states in synthetic cells.

For piPDDS-I synthetic cells, the GUV assays were prepared following the aforementioned procedures, with the exception of the inner solution, which contained 300 mM sucrose, 10 mM Mg^{2+}, L_iL_i' (0.40 μM), A_1A_1' (0.08 μM), B_1B_1' (0.08 μM), D (0.08 μM), T_1 (0.08 μM), T_2 (0.08 μM), F_2Q_2 (1.0 μM), F_3Q_3 (1.0 μM), each NTP (5.72 mM), and T7 RNAP (0.95 $U \cdot \mu L^{-1}$). The prepared GUVs were then irradiated with UV light (365 nm, 3 $mW \cdot cm^{-2}$) for varying durations (0, 0.8, 1.6, 2.0, 3.0, and 4.0 min). After incubation at 37 °C for 2 h, fluorescence images were captured via a Zeiss Axio Scope A1 microscope and processed with ImageJ.

For piPDDS-II synthetic cells, the GUV assays were prepared following the aforementioned procedures, with the exception of the inner solution, which contained 300 mM sucrose, 10 mM Mg^{2+}, L_iL_i' (0.40 μM), A_1 (0.08 μM), B_1B_2' (0.08 μM), B_2' (0.08 μM), C_1C_2' (0.08 μM), D (0.08 μM), T_1 (0.08 μM), T_2 (0.08 μM), T_3 (0.08 μM), F_2Q_2 (1.0 μM), F_3Q_3 (1.0 μM), each NTP (5.72 mM), and T7 RNAP (0.95 $U \cdot \mu L^{-1}$). The prepared GUVs were then irradiated with UV light (365 nm, 3 $mW \cdot cm^{-2}$) for varying durations (0, 1.6, 2.5, 3.0, 4.5, 5.0, and 6.0 min). After incubation at 37 °C for 2 h, fluorescence images were acquired using a Zeiss Axio Scope A1 microscope and analysed using ImageJ.

For piPDDS-III synthetic cells, the GUV assays were prepared following the aforementioned procedures, with the exception of the inner solution, which contained 300 mM sucrose, 10 mM Mg^{2+}, L_iL_i' (0.80 μM), A_1A_1' (0.08 μM), B_1B_1' (0.08 μM), C_1C_1' (0.08 μM), D (0.08 μM), T_1 (0.08 μM), T_2 (0.08 μM), T_4 (0.08 μM), F_2Q_2 (1.00 μM), F_3Q_3 (1.00 μM), F_4Q_4 (1.00 μM), each NTP (5.72 mM), and T7 RNAP (0.95 $U \cdot \mu L^{-1}$). The prepared GUVs were then irradiated with UV light (365 nm, 3 $mW \cdot cm^{-2}$) for

varying durations (0, 0.8, 1.6, 2.5, 3.0, 4.0, 6.0, and 8.0 min). After incubation at 37 °C for 2 h, fluorescence images were captured via a Zeiss Axio Scope A1 microscope and processed with ImageJ.

Probing light-duration decoding driven differential protein synthesis in synthetic cells.
For synthetic cells containing the integrated piPDDS-I/GFP-regulating riboswitch architecture, the GUV assays were prepared following the aforementioned procedures, with the exception of the inner solution, which contained 300 mM sucrose, 10 mM Mg^{2+}, L_iL_i' (0.40 μM), A_1A_1' (0.08 μM), B_1B_1' (0.08 μM), D (0.08 μM), T_1 (0.08 μM), T_2 (0.08 μM), and RNase inhibitor (0.80 $U\cdot\mu L^{-1}$), together with PURExpress enriched with 500 $ng\cdot\mu L^{-1}$ rS_1. The prepared GUVs were then irradiated with UV light (365 nm, 3 $mW\cdot cm^{-2}$) for varying durations (0, 0.8, 1.6, 2.5, 3.0, and 4.0 min). After incubation at 37 °C for 2 h, fluorescence images were acquired using a Zeiss Axio Scope A1 microscope and analysed using ImageJ.

For synthetic cells containing the integrated piPDDS-II/GFP-regulating riboswitch architecture, the GUV assays were prepared following the aforementioned procedures, with the exception of the inner solution, which contained 300 mM sucrose, 10 mM Mg^{2+}, L_iL_i' (0.40 μM), A_1 (0.08 μM), B_1B_2' (0.08 μM), B_2' (0.08 μM), C_1C_2' (0.08 μM), D (0.08 μM), T_1 (0.08 μM), T_2 (0.08 μM), T_3 (0.08 μM), and RNase inhibitor (0.80 $U\cdot\mu L^{-1}$), together with PURExpress enriched with 500 $ng\cdot\mu L^{-1}$ rS_1. The prepared GUVs were then irradiated with UV light (365 nm, 3 $mW\cdot cm^{-2}$) for varying durations (0, 1.6, 2.5, 3.0, 4.5, 5.0, and 6.0 min). After incubation at 37 °C for 2 h, fluorescence images were captured via a Zeiss Axio Scope A1 microscope and processed with ImageJ.

For synthetic cells containing the integrated piPDDS-III/GFP- and mCherry-regulating riboswitch architecture, GUV assays were prepared following the aforementioned procedures, with the exception of the inner solution, which contained 300 mM sucrose, 10 mM Mg^{2+}, L_iL_i' (0.80 μM), A_1A_1' (0.08 μM), B_1B_1' (0.08 μM), C_1C_1' (0.08 μM), D (0.08 μM), T_1 (0.08 μM), T_2 (0.08 μM), T_4 (0.08 μM), and RNase inhibitor (0.80 $U\cdot\mu L^{-1}$), together with PURExpress enriched with 500 $ng\cdot\mu L^{-1}$ rS_1 and 600 $ng\cdot\mu L^{-1}$ rS_2. The prepared GUVs were then irradiated with UV light (365 nm, 3 $mW\cdot cm^{-2}$) for varying durations (0, 0.8, 1.6, 2.5, 3.0, 4.0, 6.0, and 8.0 min). After incubation at 37 °C for 2 h, fluorescence images were acquired using a Zeiss Axio Scope A1 microscope and analysed using ImageJ.

Probing duration-windowed membrane permeabilisation in synthetic cells. To prepare synthetic cells containing the integrated piPDDS-I/α-HL-regulating riboswitch architecture, GUV assays were prepared following the aforementioned procedures, with the exception of the inner solution, which contained 300 mM sucrose, 10 mM Mg^{2+}, L_iL_i' (0.80 μM), A_1' (0.16 μM), A_1A_1' (0.08 μM), B_1B_1' (0.08 μM), D (0.08 μM), T_1 (0.08 μM), T_2 (0.08 μM), RNase inhibitor (0.80 $U\cdot\mu L^{-1}$) and Cy5 (1.00 μM), together with PURExpress enriched with 600 $ng\cdot\mu L^{-1}$ rS_3. The prepared GUVs were then irradiated with UV light (365 nm, 3 $mW\cdot cm^{-2}$) for varying durations (0, 1.6, 2.4, 3.2, 4.0, 6.0, and 8.0 min). After incubation at 37 °C for 2 h, cholesterol-modified DNA (Chol-DNA, 0.40 μM) was added for membrane labelling. Fluorescence images were captured via a Zeiss Axio Scope A1 microscope and processed with ImageJ.

Data availability

All data generated and analysed during this study are included in the published article and its Supplementary Information. Source data are provided with this paper.

Acknowledgments

This work was financially supported by the National Key Research and Development Project (no. 2021YFA0909400), the Fundamental and Interdisciplinary Disciplines Breakthrough Plan of the Ministry of Education of China (no. JYB2025XDXM602), the Open Project of State Key Laboratory of Supramolecular Structure and Materials (no. sklssm202611), and the Open Fund Project of State Key Laboratory of Synthetic Biology (no. HSK202603).

Author contributions

L.Y. led the project. S.W. and L.Y. conceived and supervised the study. S.C. and H.O. performed the experiments. All authors contributed to the design of the study, data analysis, and writing of the paper.

Competing interests

The authors declare no competing interests.

Additional information

Supplementary information The online version contains supplementary material available at

Correspondence and requests for materials should be addressed to Liang Yue.

Supplementary Files

This is a list of supplementary files associated with this preprint. Click to download.

- SupplementaryInformation.pdf